Optimization of a customized simultaneous algebraic reconstruction technique algorithm for phase-contrast breast computed tomography

S Donato[1,2] ⓘ, **L Brombal**[3,*] ⓘ, **L M Arana Peña**[3,4,5] ⓘ, **F Arfelli**[3,4], **A Contillo**[5], **P Delogu**[6,7], **F Di Lillo**[5], **V Di Trapani**[4], **V Fanti**[8,9] ⓘ, **R Longo**[3,4], **P Oliva**[9,10] ⓘ, **L Rigon**[3,4], **L Stori**[8], **G Tromba**[5] and **B Golosio**[8,9]

1   Department of Physics, University of Calabria, I-87036 Arcavacata di Rende (CS), Italy
2   INFN Division of Frascati, I-00044 Frascati (Roma), Italy
3   INFN Division of Trieste, I-34127 Trieste (TS), Italy
4   Department of Physics, University of Trieste, I-34127 Trieste (TS), Italy
5   Elettra-Sincrotrone Trieste S.C.p.A., I-34149 Trieste (TS), Italy
6   Department of Physical Sciences, Earth and Environment, University of Siena, I-53100 Siena (SI), Italy
7   INFN Division of Pisa, I-56127 Pisa (PI), Italy
8   Department of Physics, University of Cagliari, I-09042 Monserrato (CA), Italy
9   INFN Division of Cagliari, I-09042 Monserrato (CA), Italy
10   Department of Chemistry and Pharmacy, University of Sassari, I-07100 Sassari (SS), Italy
*   Author to whom any correspondence should be addressed

Abstract

Objective. To introduce the optimization of a customized GPU-based simultaneous algebraic reconstruction technique (cSART) in the field of phase-contrast breast computed tomography (bCT). The presented algorithm features a 3D bilateral regularization filter that can be tuned to yield optimal performance for clinical image visualization and tissues segmentation. *Approach.* Acquisitions of a dedicated test object and a breast specimen were performed at Elettra, the Italian synchrotron radiation (SR) facility (Trieste, Italy) using a large area CdTe single-photon counting detector. Tomographic images were obtained at 5 mGy of mean glandular dose, with a 32 keV monochromatic x-ray beam in the free-space propagation mode. Three independent algorithms parameters were optimized by using contrast-to-noise ratio (CNR), spatial resolution, and noise texture metrics. The results obtained with the cSART algorithm were compared with conventional SART and filtered back projection (FBP) reconstructions. Image segmentation was performed both with gray scale-based and supervised machine-learning approaches. *Main results.* Compared to conventional FBP reconstructions, results indicate that the proposed algorithm can yield images with a higher CNR (by 35% or more), retaining a high spatial resolution while preserving their textural properties. Alternatively, at the cost of an increased image 'patchiness', the cSART can be tuned to achieve a high-quality tissue segmentation, suggesting the possibility of performing an accurate glandularity estimation potentially of use in the realization of realistic 3D breast models starting from low radiation dose images. *Significance.* The study indicates that dedicated iterative reconstruction techniques could provide significant advantages in phase-contrast bCT imaging. The proposed algorithm offers great flexibility in terms of image reconstruction optimization, either toward diagnostic evaluation or image segmentation.

1. Introduction

X-ray breast computed tomography (bCT) is a fully 3D mammographic technique in which multiple low-dose projections are acquired over an angle of 180 degrees or more and then reconstructed through suitable

algorithms (Chen and Ning 2002, Sarno *et al* 2015, O'Connell *et al* 2018). Even though the first clinical studies in bCT were published more than ten years ago (Lindfors *et al* 2008), the integration of this technique into clinical practice has started only in recent years(Wienbeck *et al* 2017). Preliminary clinical studies have suggested that bCT can provide a good visualization of both masses and microcalcifications with a radiation dose comparable to, or slightly higher than, conventional mammographic exams (Shim *et al* 2020). Following the first generation of bCT scanners, which was based on cone-beam geometry and flat-panel detectors (Lindfors *et al* 2010, O'Connell *et al* 2010), a new generation of bCT systems based on fan beams and photon-counting detectors has been recently developed (Kalender *et al* 2017), reducing the negative impact of scattered radiation in the final image and improving the system's dose efficiency.

In addition to conventional x-ray imaging that relies uniquely on the absorption properties of the sample, phase-contrast (PhC) imaging techniques have demonstrated improved visibility of low-contrast features in soft tissues (Wilkins *et al* 1996, Mittone *et al* 2018, Brombal 2020a). In this context, programs of phase-contrast bCT (PhC bCT) are under development at Elettra, the Italian synchrotron radiation (SR) facility (Trieste, Italy) (Longo *et al* 2019), and at the Australian Synchrotron in Melbourne (Gureyev *et al* 2019). The setup at Elettra includes a high-resolution CdTe photon-counting detector (Bellazzini *et al* 2013) and it is based on the free-space propagation modality which is arguably the simplest phase-sensitive technique to implement, only requiring increasing the sample-to-detector distance to detect phase effects. Owing to the high coherence provided by a synchrotron source, this arrangement results in images with an enhanced contrast across interfaces (edge-enhancement) (Wilkins *et al* 1996). The 'edge-enhanced' images, or projections, are further processed via a phase-retrieval algorithm (Paganin *et al* 2002). The combined effect of free-space propagation and phase retrieval results in a major decrease in image noise at similar contrast and spatial resolution levels that would be observed in a conventional x-ray attenuation-based tomography (Baran *et al* 2017, Gureyev *et al* 2017, Brombal *et al* 2018a). As recently demonstrated, the image quality of PhC bCT outperforms clinical bCT systems, providing a higher spatial resolution, signal-to-noise ratio, and a finer granularity (Brombal *et al* 2019, Pacilè *et al* 2019). With the goal of setting up a clinical study, the SYRMA-3D collaboration has been working in the last years to evaluate, quantify and optimize the main parameters of the PhC bCT imaging technique in terms of x-ray energy (Delogu *et al* 2019, Oliva *et al* 2020), sample-to-detector distance (Brombal *et al* 2018b, Brombal 2020b), detector's operating mode, strategies for CT scans and reconstruction workflow (Longo *et al* 2019, Brombal *et al* 2021).

Breast computed tomography must provide high spatial and contrast resolution with a radiation dose level comparable to a standard 2-view mammography. Low radiation dose can be achieved either by reducing the x-ray fluence per tomographic projection (Greffier *et al* 2015, Solomon *et al* 2017) or by decreasing the number of projections (Sidky *et al* 2014). The first approach, while preserving a good angular sampling, results in increased noise in the projection images leading to a noisier CT image. Conversely, when the number of projections falls significantly below the Nyquist angular sampling criterion, analytical reconstruction algorithms introduce significant image artefacts and, again, increased noise. Several approaches have been proposed to improve the global image quality in low dose CT scans and some of them have been applied to bCT data (Zhao *et al* 2012), including iterative reconstruction (IR) algorithms (Sidky and Pan 2008, Makeev and Glick 2013, Bian *et al* 2014, Pacilè *et al* 2015, Delogu *et al* 2017a).

IR techniques usually search for a smooth/regular solution compatible with the measured projection data and, for some algorithms, that satisfies other additional constraints (e.g. non-negativity). Thanks to the advancements in terms of computational power, IRs are attracting a growing interest in many applications of biomedical x-ray imaging (Löve *et al* 2013, Nishiyama *et al* 2016). Multiple clinical studies have shown their potential in terms of image quality improvement and/or radiation dose reduction when compared to the standard filtered back projection (FBP) or Feldkamp–Davis–Kress reconstructions (Gervaise *et al* 2012, Löve *et al* 2013, Willemink *et al* 2013, Chen *et al* 2014a, Mirone *et al* 2014, Greffier *et al* 2015, Nishiyama *et al* 2016). Additionally, the integration of regularization filters within IR techniques enables both a noise reduction in homogeneous regions of the image (low spatial frequency component) and the preservation of details across interfaces (high spatial frequency component). On the other hand, IRs are generally associated with an undesired change in the image texture, described by radiologists as patchy (Schulz *et al* 2013, Chen *et al* 2014b), in some cases leading to a negative impact on their clinical implementation (Miéville *et al* 2013). The image 'patchiness' can be understood quantitatively as an increment of noise spatial correlation, described by a shift towards the lower spatial frequencies of the noise power spectrum (NPS) peak when compared to the FBP case.

In this framework, the reconstruction algorithm optimization represents one of the last steps of the SYRMA-3D project towards the clinical implementation of PhC bCT aiming to improve the global image quality for clinical compatible low dose CT scans, i.e. below 5 mGy of total mean glandular dose (MGD) (Fedon *et al* 2015, Mettivier *et al* 2015). In this study, we describe and use a custom-made GPU-based simultaneous algebraic reconstruction technique (cSART) in combination with a 3D bilateral regularization filter. Compared to other iterative algorithms, SART generally ensures fast convergence and flexibility allowing the implementation of

custom modifications, it is easily parallelizable on GPU and it is usually associated with noise reduction while preserving the sharpness of edges and interfaces. It should also be remarked that, despite this study being focused on SART due to its straightforward implementation, the bilateral filter can be in principle integrated within any iterative reconstruction algorithm. To date, only a few specific studies on IRs dedicated to bCT have been published (Sidky and Pan 2008, Oliva *et al* 2017, Tseng *et al* 2020) and most of the clinical applications reported in the literature rely on analytical reconstructions. The proposed cSART algorithm requires the tuning of 3 independent parameters, providing higher flexibility with respect to the standard SART (Gordon *et al* 1970, Kak *et al* 2002). Specifically, following the preliminary results published in (Donato *et al* 2019a), the effect of these parameters on NPS, spatial resolution, and contrast-to-noise ratio (CNR) are herein discussed and, by analyzing the peak frequency of the NPS curve, optimal combinations of parameters preserving the image texture are identified for the PhC bCT system at hand. Moreover, the possibility of obtaining suitable images for tissue segmentation is quantitatively investigated by using segmentation algorithms based on both gray-scale thresholding and supervised machine-learning. This task can be of great interest for the glandularity assessment and for the realization of realistic virtual (Caballo *et al* 2018) or 3D printed (Germann *et al* 2020) breast phantoms. The imaging results obtained with the cSART algorithm are compared with conventional SART and FBP reconstructions.

2. Materials and methods

2.1. Samples description
The presented study is based on images of two samples: (i) a breast mastectomy with a maximum diameter of 9 cm and a vastly differentiated infiltrating ductal carcinoma (already described in Piai *et al* 2019); (ii) a bCT dedicated test object (Contillo *et al* 2018, Piai *et al* 2019) composed by a polymethyl methacrylate (PMMA) cylindrical container (diameter 12 cm, height 10 cm) filled with demineralized water and a set of five plastic rods (diameter 1.2 cm) made of polyethylene (PE), nylon, polyoxymethylene (POM), polytetrafluoroethylene (PTFE) and BR12 breast-tissue equivalent material, respectively. These materials were chosen to mimic the attenuation and contrast of breast tissues. The test object's design allows imaging the plastic rods, for CNR and spatial resolution measurements, and the uniform water background, located at a different vertical position, for NPS evaluation. Prior to the CT scan, the mastectomy sample was fixed in formalin and sealed in a vacuum bag.

2.2. Beamline description and experimental setup
Images were collected at the SYRMEP beamline (Tromba *et al* 2010) of the Elettra synchrotron facility, with the storage ring operating at 2.4 GeV. X-rays are produced by a bending magnet and they can be monochromatized in the range 8.5–40 keV by means of a Si(111) double-crystal monochromator, providing an energy resolution of approximately 0.1%. Samples were positioned in a pendant geometry hanging from the patient support, a rotating table with an ergonomically designed aperture at the rotation center, 30 m away from the source. At the sample position, the x-ray beam had a laminar shape with a cross-section of 220 mm (horizontal) $\times$ 3.5 mm (vertical, Gaussian shape, full width half maximum), while the object-to-detector distance was set to 1.6 m. Images were collected with a CdTe photon-counting detector (Pixirad-8) (Bellazzini *et al* 2013, Delogu *et al* 2017b) featuring a 60 μm pixel pitch and a global active area of 246 mm $\times$ 24.8 mm, leading to a matrix of 4096 $\times$ 476 pixels. Samples were scanned in continuous rotation by acquiring 1200 evenly spaced projections over 180° at a rate of 30 Hz. The beam energy was set to 32 keV while the beam intensity was adjusted by means of aluminum filters to deliver 5 mGy of total MGD.

2.3. Image reconstruction
Projection images were pre-processed through a detector-specific procedure (Brombal *et al* 2018c) and phase-retrieved prior to tomographic reconstruction (Brombal *et al* 2018b, Donato *et al* 2019b). The well-known phase-retrieval algorithm based on the homogeneous transport of intensity equation (TIE-Hom) (Paganin *et al* 2002) was used, selecting a δ/β value of 2308, which corresponds to (ICRU-44) breast tissue (White *et al* 1989), as reported in a publicly available database (Taylor 2018). Phase-retrieved projections were reconstructed with a GPU-based FBP and Shepp–Logan filtering, a standard SART with 5 iterations -both part of the Astra toolbox for tomography (Van Aarle *et al* 2016) - and the cSART algorithm introduced in the next section. In addition to the Shepp–Logan filtering, which is standard in many bCT applications (Brombal *et al* 2019, Shim *et al* 2020), reconstructions with different common FBP filters were performed. Namely, from the sharpest to the smoothest, Ram-Lak, Cosine, Hamming, and Hann, filters were used and the respective results are reported in the supplementary material (available online at stacks.iop.org/PMB/67/095012/mmedia). Reconstructions were performed on a system equipped with a GPU NVIDIA® GeForce RTX 2080 Ti card with 11 GB of GDDR6 VRAM, 4352 CUDA cores, and a boost clock of 1.635 MHz. The reconstruction time for each slice was: 25 s for the cSART, 21 s for the standard SART, and less than 1 s for FBP.

2.4. The custom SART algorithm

(i) The iterative corrections are weighed with a relaxation factor (Golosio *et al* 2004), so that the update formula for the $(k+1)$th iteration reads:

$$F^{(k+1)}(i_x, i_y) = F^{(k)}(i_x, i_y) + \eta^{(k)} C^{(k)}(i_x, i_y), \tag{1}$$

where $F^{(k)}$ is the image estimated at the kth iteration and $C^{(k)}$ is the respective normalized image correction in the reconstruction plane (i_x, i_y). The relaxation factor η is applied to the corrections to reduce image noise in the reconstruction. In our implementation, η grows linearly from zero to a maximum $\eta_{\max}$ in the first few angular steps (in the current work this value was set to 10) then it decreases linearly with the number of iterations and angular steps down to zero for the last angular step of the last iteration. In this work we used $\eta_{\max} = 0.5$.

(ii) Projections corresponding to different angles are used in a random ordering scheme.

(iii) A bilateral 3D filter is applied periodically to the reconstructed image guess during the iterative process. In the filter, the content of each pixel is replaced with a weighted average accounting for both the (3D) Euclidean distance and the gray-level difference of neighboring pixels. The used weighting kernels are Gaussian, so that the weight of the pixel identified with indices i_x', i_y', i_z' in filtering the pixel i_x, i_y, i_z is:

$$K(i_x', i_y', i_z'; i_x, i_y, i_z) = \exp\left[-\frac{(i_x' - i_x)^2 + (i_y' - i_y)^2}{2\sigma_{xy}^2} \dots \right.$$
$$\left. -\frac{(i_z' - i_z)^2}{2\sigma_z^2} - \frac{(F(i_x', i_y', i_z') - F(i_x, i_y, i_z))^2}{2\sigma_v^2} \right], \tag{2}$$

where σ_{xy}, σ_z and σ_v are parameters related to the spatial width of the filter in the horizontal plane, to the width in vertical direction, and to the width in content difference, respectively. $F(i_x', i_y', i_z')$ and $F(i_x, i_y, i_z)$ are the contents of the pixels i_x', i_y', i_z' and i_x, i_y, i_z respectively, where x and y are the spatial coordinates in each projection image and z is the projection index. In this work σ_{xy} and σ_z are chosen to be equal and expressed in pixel size units, while σ_v is expressed in the same units as $F(i_x, i_y, i_z)$. By calling $\tilde{F}^{(k)}$ the image filtered with the kernel K, the reconstructed image is updated periodically during the iterative process as:

$$F^{(k)} \rightarrow (1 - w) F^{(k)} + w \tilde{F}^{(k)}, \tag{3}$$

where w is a weighting factor comprised between 0 (no filtration) and 1 (full filtration).

To optimize the cSART parameters, images were reconstructed with different combinations of the algorithm's parameters, by varying $\sigma_{xy} = \sigma_z$ in the range [2: 7] pixels with a step of 1 pixel, σ_v in the range [0.004: 0.014] with a step of 0.002 and w in the range [0.04: 0.16] with a step of 0.02, corresponding to a total of 252 reconstructions. Of note, we set $\sigma_{xy} = \sigma_z$, but in principle they can be different for a higher level of customization. The number of iterations was fixed to 5, consistently with the standard SART reconstructions, while the regularization filter was applied every 100 randomly ordered angular steps. Reconstructions were also obtained with different numbers of iterations in the range [4: 8]: in the main text only results corresponding to 5 iterations are shown, whereas results for different numbers of iterations are reported in the supplementary materials document.

2.5. Quantitative assessment

The quantitative evaluation of cSART images was carried out in comparison with the FBP algorithm, assumed as a reference, and with the standard SART algorithm. We firstly focused on the image texture by analyzing the NPS. Then a quantitative evaluation was performed by using the CNR and spatial resolution metrics. Lastly, a further type of assessment involved the use of reconstructions for tissue segmentation. Images were analyzed through dedicated MATLAB (The MathWorks, Inc., Natick, MA, United States) codes.

2.5.1. Noise power spectrum

Image noise and texture were characterized by means of the NPS (Verdun *et al* 2015), which is the noise spectral decomposition in the Fourier space. For each reconstruction the 2D NPS map was measured from equally sized homogeneous ROIs according to the following definition:
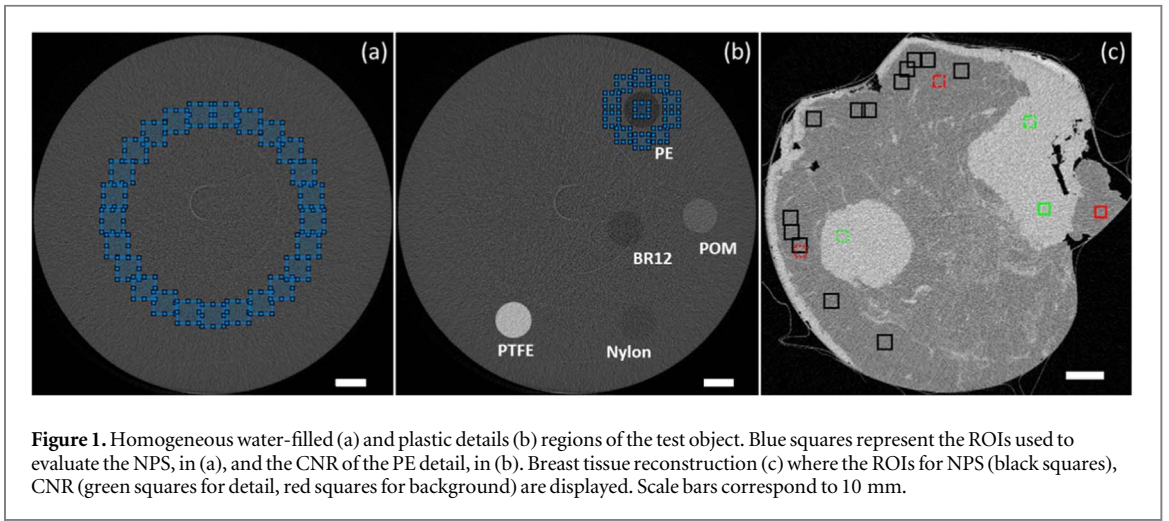
Figure 1. Homogeneous water-filled (a) and plastic details (b) regions of the test object. Blue squares represent the ROIs used to evaluate the NPS, in (a), and the CNR of the PE detail, in (b). Breast tissue reconstruction (c) where the ROIs for NPS (black squares), CNR (green squares for detail, red squares for background) are displayed. Scale bars correspond to 10 mm.

$$NPS(f_x, f_y) = \frac{d_x d_y}{N_x N_y} \frac{1}{N_{ROI}} \sum_{i=1}^{N_{ROI}} |\mathcal{F}[I_i(x, y) - \bar{I}_i]|^2, \qquad (4)$$

where f_x and f_y are the spatial frequencies, N_x and N_y are the ROI dimensions in number of pixels, d_x and d_y are the pixel dimensions in mm, N_{ROI} is the total number of selected ROIs, $\mathcal{F}$ denotes the 2D Fourier transform, $I_i(x, y)$ is the pixel value at position (x,y) of the ith ROI, while $\bar{I}_i$ is the respective mean value. The corresponding image noise (σ) is obtained from the NPS as:

$$\sigma^2 = \int \int NPS(f_x, f_y) df_x df_y. \qquad (5)$$

Given the radial symmetry of 2D NPS in CT reconstructions, 1D radially averaged NPS maps were also computed by using the identity $f_r^2 = f_x^2 + f_y^2$. Peak frequency (f_{peak}) of radial NPS curves was used for the determination of image texture, where a high peak frequency corresponds to a high granularity and a low peak frequency corresponds to a coarse noise, resulting in a patchy appearance. On the test object, both 2D and 1D NPS distributions were evaluated by selecting in a homogeneous water region 25 non-overlapping circularly distributed square ROIs with an area of 0.72×0.72 mm^2, as shown in figure 1(a). For the breast sample, NPS measurements were performed over 10 homogeneous ROIs within the adipose tissue (black squares in figure 1 (c)) at nearly the same distance from the center of the specimen. Each ROI within the tissue has 64×64 pixels area (0.36×0.36 mm^2). To precisely determine their peak frequency, 1D NPS curves were oversampled by a factor of 4.

2.5.2. Contrast-to-noise ratio
The CNR was evaluated by using the following definition:

$$CNR = \frac{\overline{I_d} - \overline{I_b}}{\sqrt{(\sigma_d^2 + \sigma_b^2)/2}}, \qquad (6)$$

where $\overline{I_d}$ and $\overline{I_b}$ are the average pixel intensities of the detail d and the background b, while σ_d and σ_b are the respective standard deviations (i.e. noise). In the phantom, the CNR of each plastic insert was measured with respect to the water background. A square ROI of 64×64 pixels was selected within each rod, while, for the background estimation, 10 evenly spaced ROIs were selected in the neighboring region (see figure 1(b)). The background's standard deviation was taken as the average of the background ROIs standard deviations. On the breast specimen, CNR was measured as the average CNR value of three pairs of square ROIs selected within glandular (detail) and adipose (background) tissues, as shown by the green and red squares in figure 1(c).

2.5.3. Spatial resolution
In the test object, the spatial resolution was characterized through the task transfer function (TTF), which is an object-dependent extension of the modulation transfer function (MTF) describing the spatial resolution for a specific object contrast and background noise (Li *et al* 2014, Solomon *et al* 2015). While MTF is usually measured on a single high-contrast detail, TTF is measured for various materials exhibiting different contrasts. TTF is useful in the characterization of nonlinear/iterative algorithms where the spatial resolution is, in general, influenced by the image contrast level, meaning that different interfaces will show different levels of sharpness. It

is worth noting that, when phase-retrieval filter is applied, this consideration applies also to FBP reconstructions and it will be discussed in more detail in section 3.1.2.

TTF was evaluated by using the circular edge method, which requires a polar coordinate transformation allowing to estimate the detail's edge-spread function from which TTF is derived (Richard *et al* 2012, Chen *et al* 2014b). TTF was measured on PE, Delrin and Teflon inserts whereas the contrast yielded by Nylon and BR12 inserts was insufficient for applying the circular edge method. Starting from the frequency corresponding to the 50% of the TTF curve ($f_{50\%}$), the spatial resolution was evaluated as the full width at half maximum (FWHM) of the corresponding point-spread function (PSF) (Bartels 2013):

$$FWHM\,(mm) = \frac{1}{2.26 \times f_{50\%}\,(lp/mm)}, \tag{7}$$

where this equation holds in the Gaussian approximation for both TTF and PSF.

Due to the lack of sharp interfaces in the breast specimen, the spatial resolution was estimated through an alternative procedure recently introduced by Mizutani *et al* (2016), which has already been applied to bCT images (Brombal *et al* 2019). The main advantage of this approach, based on Fourier spectrum's fitting (Saiga *et al* 2018), is that it allows to estimate the overall spatial resolution in terms of FWHM directly from general sample images, thus not requiring dedicated test objects. On the other hand, the model underlying this method contains the assumption of a Gaussian system's PSF, which is not rigorously true for many modern CT systems, and it is not material specific. In this context, Mizutani's method can be regarded as an approximate but easy way to assess spatial resolution from general samples images that is particularly useful for comparative studies. To cross-check the spatial resolution results, this technique is also applied to the test object images.

2.5.4. Segmentation and image comparison

The last type of quantitative assessment in this study involved tissue segmentation and the comparison against a high dose (50 mGy) ground-truth FBP reconstruction. Image segmentation was performed via two different methods: (i) standard gray scale-based discrimination of tissues and (ii) supervised machine-learning for features recognition. The first approach consists in using two thresholds, one for the separation of the background (air) and the other for the separation of glandular from adipose tissues. For the ground-truth image, which presents a low level of noise, the gray-level distributions of the tissue's components are well separated, so the segmentation thresholds were set at the local minima between each distributions pair. On the other hand, the gray-level distributions of adipose and glandular tissues in the low dose images present, in general, superposition, therefore requiring for a threshold optimization. The gray-level distributions of both ground-truth and low dose images are reported in figure S1 of the supplementary material.

The second segmentation method is based on supervised machine-learning (ML), namely on a multi-threaded implementation of the fast Random Forest algorithm (Breiman 2001). The algorithm is included in the WEKA (Waikato Environment for Knowledge Analysis) trainable segmentation toolbox (Arganda-Carreras *et al* 2017) available in Fiji (Schindelin *et al* 2012), and it has been widely applied to tomographic datasets (Polan *et al* 2016, Rodrigues *et al* 2016, Wollatz *et al* 2017). The algorithm combines a series of machine learning algorithms to classify an image based on a set of training pixels selected by the user. In analogy with the gray scale-based segmentation, the training of the classifier is based on the definition of three categories, namely background, adipose, and glandular tissue, to which representative voxels are assigned. The feature extraction is performed by applying to input images different filters, namely edge detectors, texture filters, noise reduction filters, and membrane detectors. The selection of the filters influences the way the fast Random Forest decision trees classify the remaining pixels. Specifically, based on a trial-and-error process, classification was performed by selecting Gaussian blur, Sobel, Hessian, difference of Gaussians, membrane projections, Kuwahara, entropy, and neighbors filters, while the Random Forest classifier was set to 200 trees with unlimited depth. Once the classifier was properly trained to segment the high-dose image, it was saved and applied to low-dose images.

The figure of merit chosen for the evaluation of segmentation quality and for the optimization of reconstruction parameters and segmentation thresholds was the macro-$F1$ score (Opitz and Burst 2019). This score is often used in multi-class classification problems (Lipton *et al* 2014, Wu and Zhou 2017) and it is based on the image confusion matrix. In particular, let m_{ij} be the element i, j of the confusion matrix, where the second index j represents the ground-truth, while the first index i represents the output of the classification. In our application, m_{ij} is the number of pixels that belong to class j in the segmented high-dose image and to class i in the segmented low-dose image. Let P_i, R_i and $F1_i$ denote the precision, recall, and $F1$ score for the class i:

$$P_i = \frac{m_{ii}}{\sum_j m_{ij}}; \quad R_i = \frac{m_{ii}}{\sum_j m_{ji}}; \quad F1_i = \frac{2P_i R_i}{P_i + R_i}. \tag{8}$$
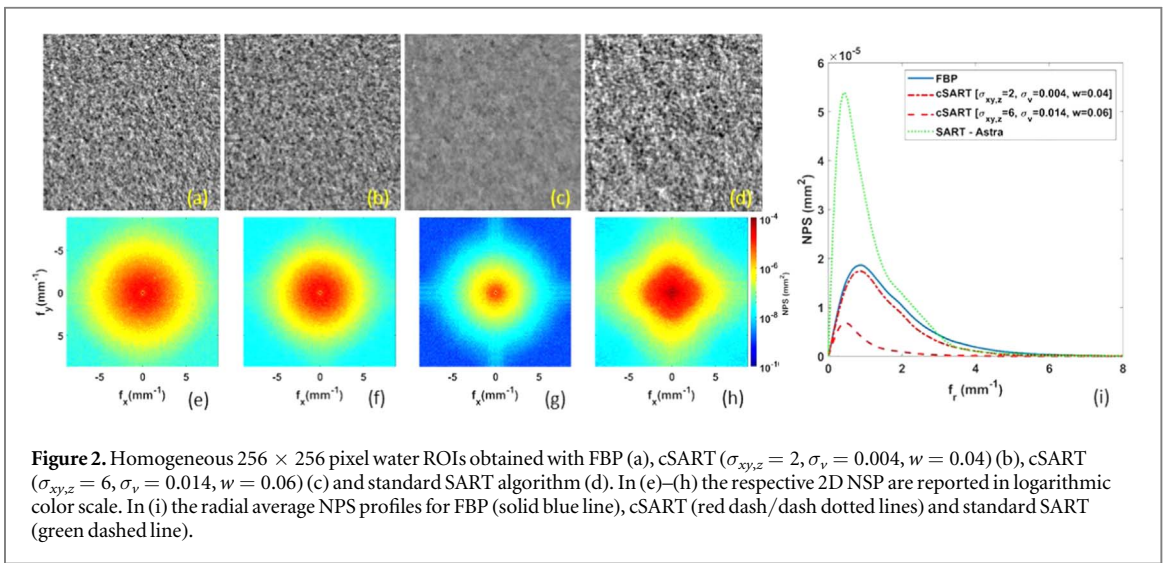
Figure 2. Homogeneous 256 × 256 pixel water ROIs obtained with FBP (a), cSART ($\sigma_{xy,z} = 2$, $\sigma_v = 0.004$, $w = 0.04$) (b), cSART ($\sigma_{xy,z} = 6$, $\sigma_v = 0.014$, $w = 0.06$) (c) and standard SART algorithm (d). In (e)–(h) the respective 2D NSP are reported in logarithmic color scale. In (i) the radial average NPS profiles for FBP (solid blue line), cSART (red dash/dash dotted lines) and standard SART (green dashed line).

The macro-$F1$ is computed as the arithmetic mean of the $F1$ scores of all the classes:

$$F1 = \frac{1}{n} \sum_i F1_i, \tag{9}$$

where n is the number of classes. Given its definition, the values of $F1$ range from 0 to 1, with 1 indicating a segmentation identical to the ground truth. The optimal cSART reconstruction in terms of segmentation will be the one that maximizes $F1$ with respect to all the four free parameters, namely $\sigma_{xy,z}$, σ_v, η, and the threshold th between glandular and adipose components. In this analysis, the range of cSART reconstruction parameters has been further expanded by varying σ_{xy} and σ_z in the range [2: 10] pixels with a step of 1 pixel, σ_v in the range [0.004: 0.030] with a step of 0.002 and w in the range [0.04: 0.20] with a step of 0.02.
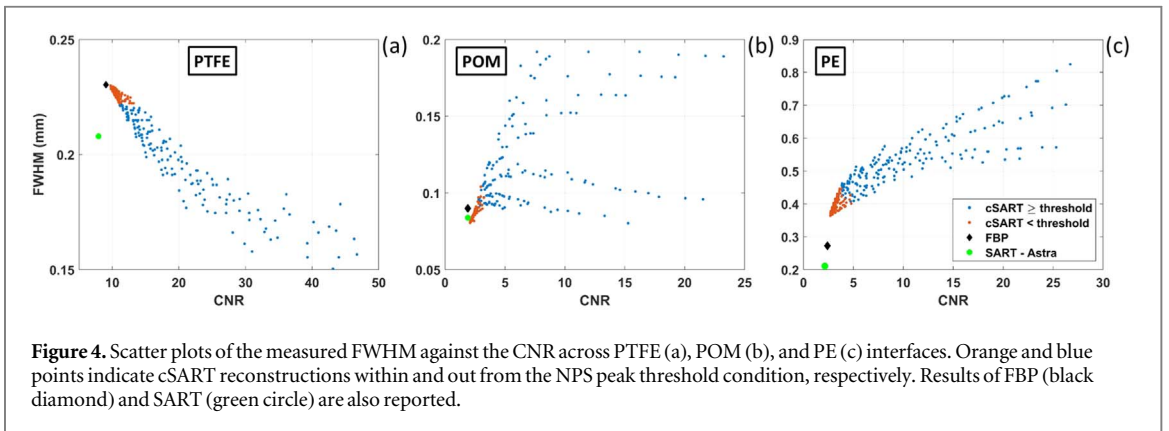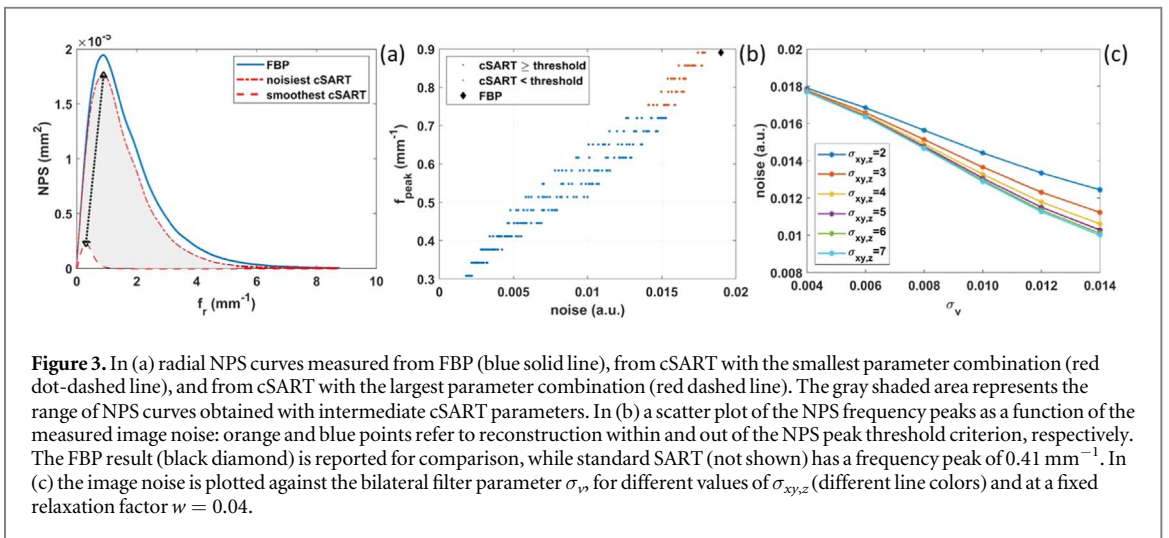
3. Results and discussion

3.1. Test object

3.1.1. Noise power spectrum

As stated in the introduction, the shift toward low frequencies of the NPS peak is followed by a change in the image texture demonstrated in figure 2. Panels (a)–(d) show homogeneous water ROIs reconstructed with FBP, cSART (with $\sigma_{xy,z} = 2$, $\sigma_v = 0.004$ and $w = 0.04$), cSART (with $\sigma_{xy,z} = 6$, $\sigma_v = 0.014$ and $w = 0.06$) and standard SART, respectively. Their respective 2D NPS plots are reported in color logarithmic scale in panels (e)–(h). The 2D NPS plots of FBP and cSART show a clear circular symmetry, while in the SART case a slightly higher noise contribution is observed along the Cartesian directions. From 2D NPS plots the average radial profiles are computed as shown in panel (i), resulting in peak frequencies of 0.89 mm^{-1}, 0.89 mm^{-1}, 0.44 mm^{-1}, and 0.44 mm^{-1}, respectively. In terms of texture, it is clear that the cSART with low parameters values allows producing images that are very similar to the reference FBP case, whereas larger values, as well as the use of standard SART, introduce more correlation resulting in a coarser noise. On the other hand, the cSART algorithm allows a reduction (by a factor larger than 2 with the largest parameters values) in the noise magnitude if compared with the FBP. Conversely, the standard SART yields a higher noise than FBP. Considering that in SART reconstructions the noise magnitude decreases for smaller iteration numbers, additional reconstructions have been performed with a decreasing number of iterations (from 5 to 1) but little differences (below 10%) in noise magnitude were found.

Focusing on the optimization of cSART parameters, panel (a) of figure 3 shows the radial NPS behavior going from the smallest (noisiest image) to the largest (smoothest image) cSART parameter combination in comparison with the FBP case. Results considering reconstructions performed with FBP filters other than Shepp–Logan are reported in figure S2 (a) of the supplementary material. The double-arrow line indicates that the NPS peak frequency moves toward lower values as the image noise decreases. This behavior is further supported by the scatter plot in panel (b) where it is shown that the NPS peak frequency is strongly correlated with (as a first approximation linearly dependent to) the image noise magnitude. Moreover, having the possibility to finely modify the NPS peak frequency by tuning the cSART parameters, it is useful to define a threshold criterion to distinguish parameters preserving a noise texture similar to the FBP case from parameter sets yielding a coarse/patchy image appearance. Consequently, in panel (b) a threshold criterion has been

Figure 3. In (a) radial NPS curves measured from FBP (blue solid line), from cSART with the smallest parameter combination (red dot-dashed line), and from cSART with the largest parameter combination (red dashed line). The gray shaded area represents the range of NPS curves obtained with intermediate cSART parameters. In (b) a scatter plot of the NPS frequency peaks as a function of the measured image noise: orange and blue points refer to reconstruction within and out of the NPS peak threshold criterion, respectively. The FBP result (black diamond) is reported for comparison, while standard SART (not shown) has a frequency peak of 0.41 mm^{-1}. In (c) the image noise is plotted against the bilateral filter parameter σ_v for different values of $\sigma_{xy,z}$ (different line colors) and at a fixed relaxation factor $w = 0.04$.

Figure 4. Scatter plots of the measured FWHM against the CNR across PTFE (a), POM (b), and PE (c) interfaces. Orange and blue points indicate cSART reconstructions within and out from the NPS peak threshold condition, respectively. Results of FBP (black diamond) and SART (green circle) are also reported.

introduced to identify images whose NPS peaks differ less than 15% from the FBP case (orange points). Despite being an arbitrary value and related to our imaging system, which can be in principle subject to dedicated optimization, this threshold is useful as first-line discrimination to rule out parameters yielding a too aggressive image filtration. Panel (c) shows the dependence of image noise versus the bilateral filter width σ_v for different values of $\sigma_{xy,z}$ at a fixed relaxation factor $\eta = 0.04$. From the figure, it is clear that larger filter parameters monotonically bring to lower image noise. The same consideration holds for increasing relaxation factor values. For this reason, each triplet of the cSART parameters identifies the image filtration 'strength', where the increase of each parameter brings to a lower noise magnitude and a lower NPS peak frequency. Similar behavior has been discussed for other iterative filters used in clinical practice in a number of recent publications (Ghetti *et al* 2013, Solomon *et al* 2015, Euler *et al* 2018).

3.1.2. CNR and spatial resolution
The scatter plots in figure 4 show the spatial resolution, measured with the circular edge technique, as a function of the CNR corresponding to the PTFE (a), POM (b), and PE (c) details, respectively, for the images reconstructed with cSART (dots), FBP (diamond marker) and SART (circular marker). Results for the different FBP filters are reported in figure S2 (b) of the supplementary material. The results show that the use of cSART algorithm can yield a significant increase in CNR which, considering only the points within the threshold condition, is as high as 45%, 70%, and 100% for PTFE, POM, and PE details, respectively. In terms of spatial resolution, the cSART yields comparable or better results with respect to the FBP for the PTFE (a) and POM (b) details, while the resolution is degraded at the PE (c) interface by a 30% or more. Considering the trends of the cSART data for the different materials, it is interesting to observe that higher CNR values are associated with better spatial resolutions at PTFE interface (a) and with a generally worse resolution at POM (b) and PE (c) interfaces. These different trends further justify the use of the TTF approach, as the results of the custom iterative reconstruction algorithm exhibit a material-specific behavior. On the same topic, it should be noted that the FWHM broadly varies as a function of the interface also for FBP reconstructions, going from 0.09 mm for POM to 0.27 mm for PE. This effect, which should not be present in conventional attenuation-based CT, is due to the
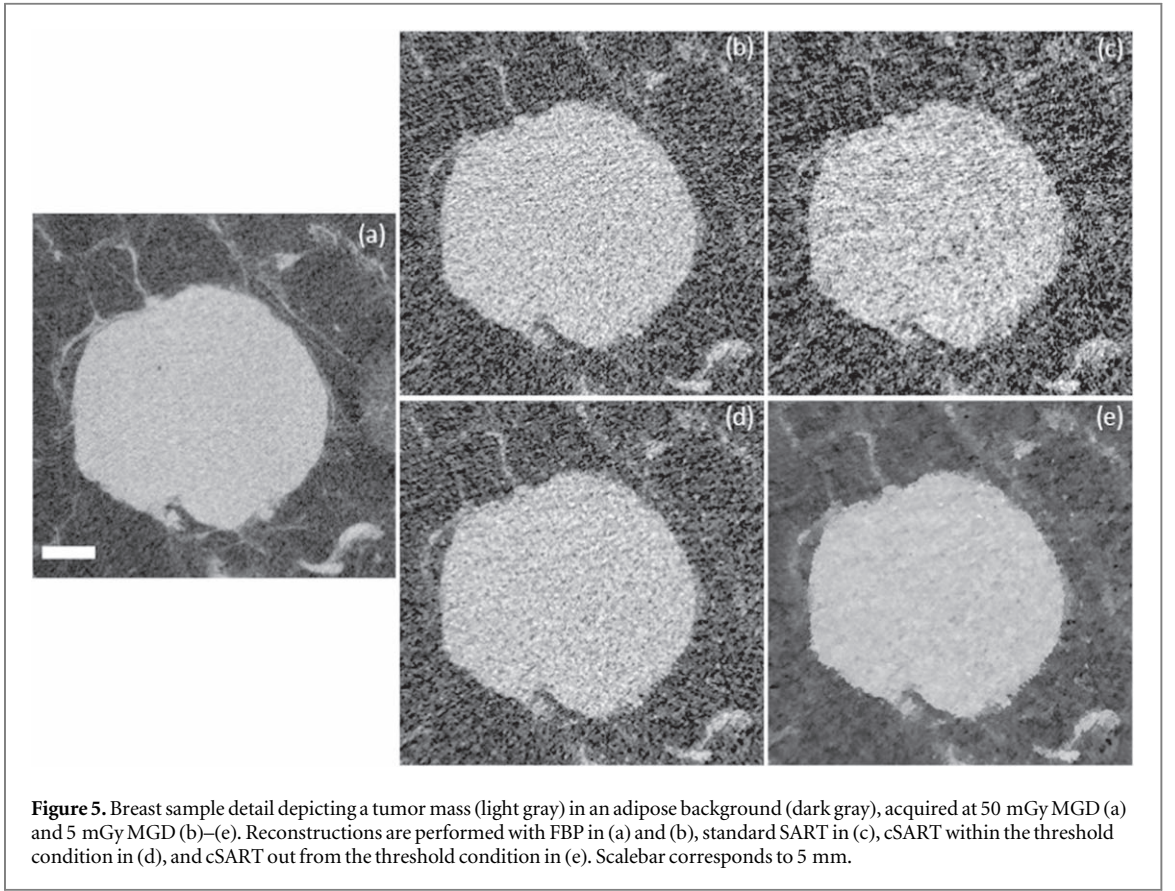
Figure 5. Breast sample detail depicting a tumor mass (light gray) in an adipose background (dark gray), acquired at 50 mGy MGD (a) and 5 mGy MGD (b)–(e). Reconstructions are performed with FBP in (a) and (b), standard SART in (c), cSART within the threshold condition in (d), and cSART out from the threshold condition in (e). Scalebar corresponds to 5 mm.

application of the phase-retrieval filter that is common to all the reconstructed images. In fact, the δ/β parameter of the phase-retrieval filter is material/interface specific. Since the scanned object is heterogeneous, the chosen δ/β cannot be optimal for all the interfaces within the sample, resulting in an excessive blurring at the interfaces where δ/β is overestimated, and an enhanced sharpness due to uncompensated phase-contrast fringes at interfaces where δ/β is underestimated (Thompson *et al* 2019). In our work, we set $\delta/\beta = 2308$, which corresponds to the breast tissue/air interface at 32 keV. On the other hand, the nominal δ/β values for the phantom inserts' interfaces with water are 1448 for PTFE, 41765 for POM, and 427 for PE, respectively. Considering that, from a signal processing perspective higher δ/β values correspond to higher smoothing due to the phase retrieval (Beltran *et al* 2010, Brombal *et al* 2018b, Donato *et al* 2019b), it is clear that the POM interface is under-smoothed, yielding the best spatial resolution, while both PTFE and PE interfaces are over-smoothed, the latter yielding the worst spatial resolution. To allow for a visual comparison the test object's images reconstructed with FBP, SART, cSART within and out from the threshold condition are reported in figures S3 and S4 of the supplementary material.

3.2. Breast specimen

3.2.1. Texture, contrast-to-noise, and spatial resolution

A qualitative comparison of a detail of the breast sample centered on the tumor mass is shown in figure 5; in panel (a) the reference image acquired at high radiation dose (50 mGy) is reported, while from (b) to (e) there are the images acquired with the standard 5 mGy dose and reconstructed through FBP (b), standard SART (c), cSART within the threshold condition (d) ($\sigma_{xy,z} = 2$, $\sigma_v = 0.008$ and $w = 0.06$) and out from the threshold condition (e) ($\sigma_{xy,z} = 7$, $\sigma_v = 0.014$ and $w = 0.08$). As expected from the photon statistics, going from the high to the low dose images reconstructed via FBP a 3-fold decrease in CNR is observed (from 9.2 to 3.1). On the other hand, no advantage over FBP in terms of image quality is associated with the use of conventional SART, while the cSART image satisfying the threshold criterion features a higher CNR (4.2), similar texture, and no apparent spatial resolution degradation. Interestingly, as shown in (e), by increasing the cSART parameters an image with the same CNR observed in the reference high dose image (CNR = 9.2) can be obtained at cost of increased patchiness. The corresponding images of the whole sample are reported in figure S5 of the supplementary material.

The quantitative analysis of the specimen images is reported in figure 6. In particular, panel (a) shows the FWHM, evaluated with Mizutani's approach, as a function of CNR measured on the breast specimen for cSART,
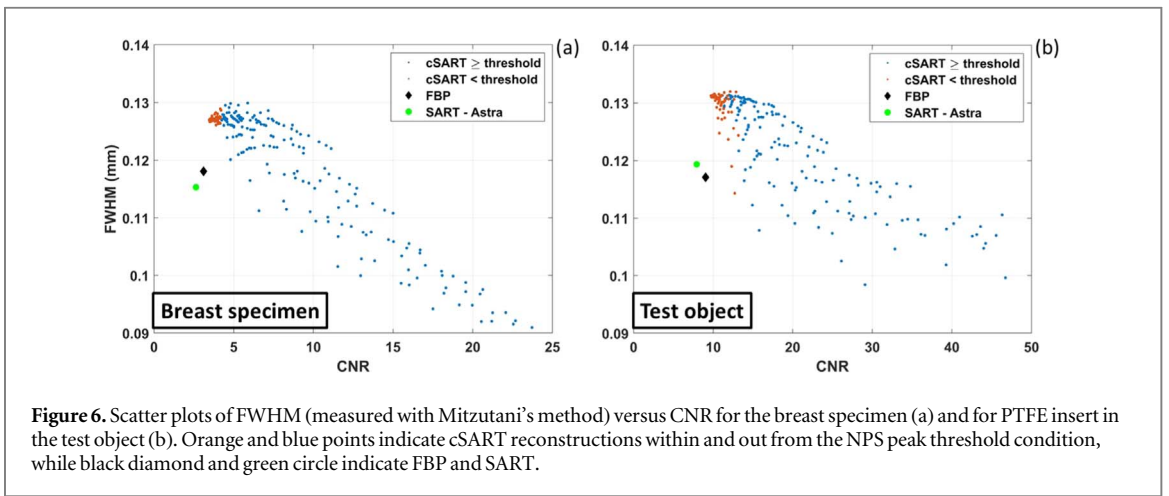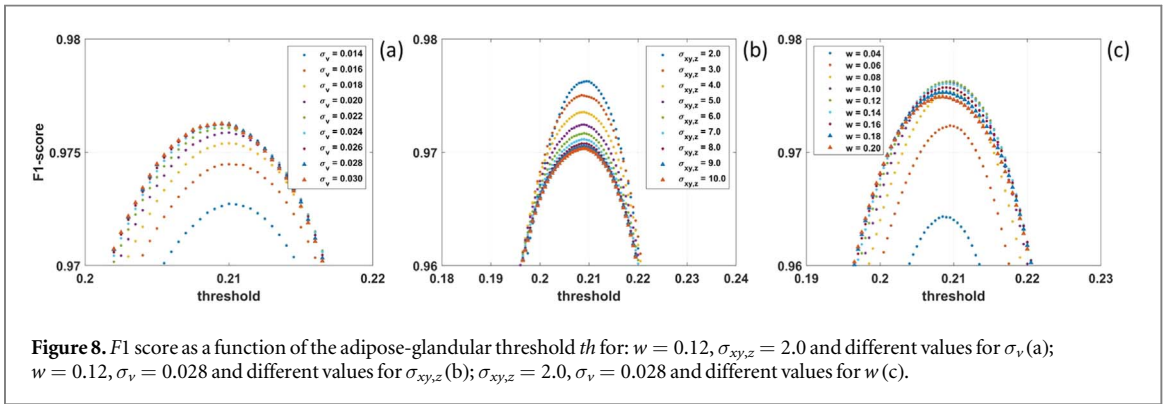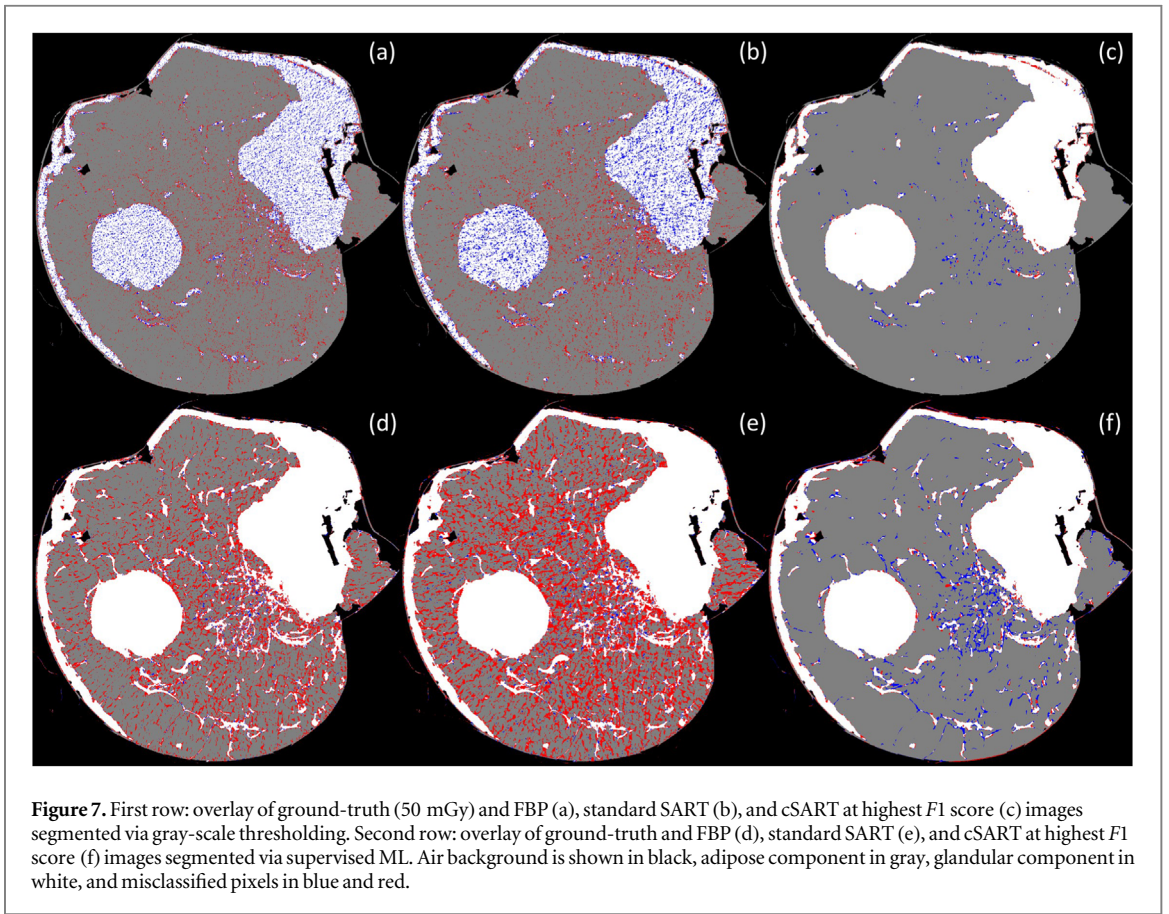
Figure 6. Scatter plots of FWHM (measured with Mitzutani's method) versus CNR for the breast specimen (a) and for PTFE insert in the test object (b). Orange and blue points indicate cSART reconstructions within and out from the NPS peak threshold condition, while black diamond and green circle indicate FBP and SART.

FBP, and SART reconstructions. Similar to the test object's case, the cSART reconstructions satisfying the NPS frequency peak threshold criterion, yield a higher CNR (up to 35%) if compared to FBP, with only a marginal degradation (below 10%) in the spatial resolution. On the other hand, the standard SART reconstruction yields a spatial resolution comparable with FBP but with a 15% lower CNR. In absolute terms, the mean FWHM of cSART reconstructions satisfying the threshold condition is 0.13 mm, whereas for the FBP case it is around 0.12 mm. The latter value is in good agreement with previous measurements performed with the same imaging setup on different samples (Brombal *et al* 2018a, Donato *et al* 2019b, Brombal *et al* 2019), and it corresponds roughly to twice the detector's pixel size. Interestingly, when applying Mizutani's approach to the test object, similar spatial resolution values are observed, as shown in panel (b). As mentioned, this approach aims at evaluating the overall spatial resolution of the imaging system, therefore it is expected that the FWHM does not change by changing the sample.

3.2.2. Image segmentation

Qualitative results of the image segmentation are shown in figure 7. Panels (a)–(c) show the overlay of the segmented ground-truth image with the segmented FBP (a), standard SART (b), and cSART at the highest *F*1 (c) images, obtained with the gray scale-based segmentation, while panels (d)–(f) show the same overlay of images segmented through supervised ML. The three components of the segmentation, namely background, adipose, and glandular tissue are shown, respectively, in black, gray, and white. Blue and red pixels are the misclassified pixels of adipose and glandular classes, where blue is glandular classified as adipose and red is vice versa. From the images, it is clear that, regardless of the segmentation approach, the cSART algorithm with adequately tuned parameters largely outperforms the FBP-based segmented image. Additionally, it is worth noting that, when comparing the two segmentation methods, the supervised ML approach is able to recognize and classify subtle image features (e.g. spiculations) which are lost in the gray scale-based segmentation, thus enabling to preserve the continuity of structures and boundaries of potential clinical interest.
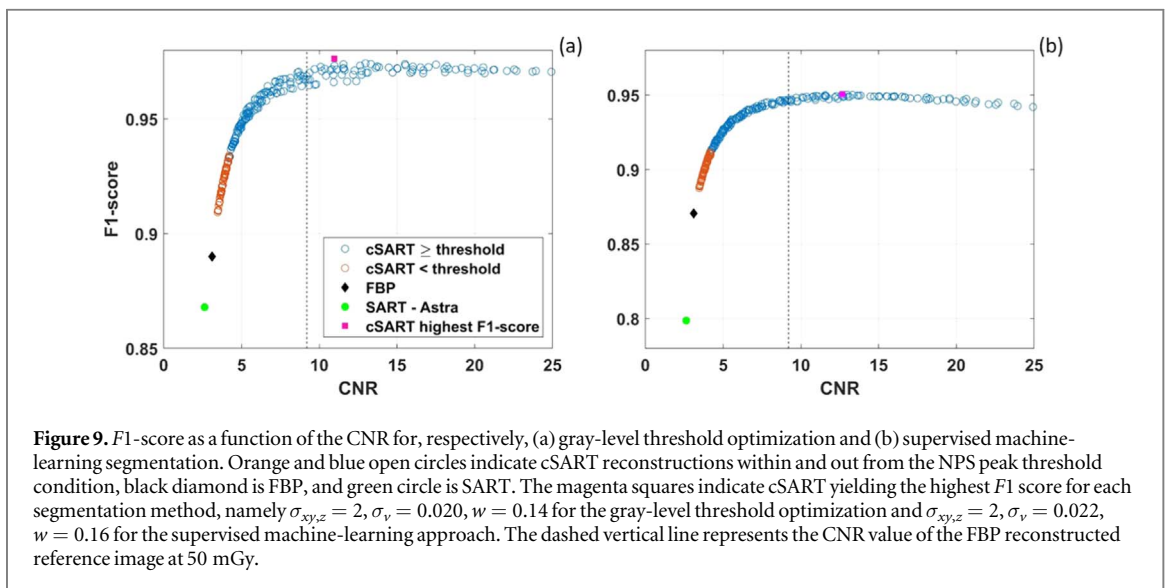
The quantitative analysis of the gray-scale threshold optimization is reported in the plots in figure 8. In panels (a)–(c) the optimization of the segmentation threshold between glandular and adipose components for different cSART parameters combinations is reported. The optimal threshold was found to be loosely independent from the reconstruction parameters and, in all cases, was around 0.21. Considering the effect of each cSART parameter on segmentation quality, panel (a) demonstrates that *F*1 increases at higher σ_v values reaching a plateau for $\sigma_v > 0.022$. Conversely, panel (b) shows that higher *F*1 scores are related to lower $\sigma_{xy,z}$, hence to small spatial blurring which contributes to the preservation of fine details. Finally, panel (c) shows that *F*1 peaks for intermediate values of *w*. In figure 9 the *F*1 scores are plotted against the respective CNR values, also including the FBP and SART reconstructions, for the gray scale-based segmentation (a) and for the supervised ML segmentation (b). Independently from the chosen segmentation approach, the plots indicate that cSART reconstructions always result in a better segmentation with respect to FBP and SART. Moreover, it is interesting to observe that a higher fidelity in the segmentation is achieved for cSART reconstructions not comprised within the NPS frequency peak threshold condition, indicating that optimal parameters for segmentation are different with respect to the ones for diagnostic visualization. The plots also indicate that when the cSART images reach the same CNR as the reference image (dashed line) the segmentation quality saturates and there is no advantage in pursuing higher CNR values. In addition, segmentation results obtained with the cSART algorithm for different numbers of iterations, from 4 to 8, are reported in figure S6 of the supplementary material and in supplementary table 1. The results show that the highest *F*1-score corresponds to 5 iterations, while neither the

Figure 7. First row: overlay of ground-truth (50 mGy) and FBP (a), standard SART (b), and cSART at highest *F*1 score (c) images segmented via gray-scale thresholding. Second row: overlay of ground-truth and FBP (d), standard SART (e), and cSART at highest *F*1 score (f) images segmented via supervised ML. Air background is shown in black, adipose component in gray, glandular component in white, and misclassified pixels in blue and red.

Figure 8. *F*1 score as a function of the adipose-glandular threshold *th* for: $w = 0.12$, $\sigma_{xy,z} = 2.0$ and different values for σ_v (a); $w = 0.12$, $\sigma_v = 0.028$ and different values for $\sigma_{xy,z}$ (b); $\sigma_{xy,z} = 2.0$, $\sigma_v = 0.028$ and different values for *w* (c).

optimal $\sigma_{xy,z}$ nor the optimal σ_v are dependent on the number of iterations. On the other hand, when increasing the number of iterations, the optimal weighting factor *w* tends to decrease.

4. Conclusions

This study shows that the adoption of iterative reconstruction techniques can provide significant advantages in the context of breast CT imaging with monochromatic synchrotron radiation and using free-space propagation and phase-retrieval. In particular, based on images of a surgical breast sample, the use of the customized GPU-based SART algorithm herein presented resulted in a contrast to noise ratio gain of up to 35% with an only marginal decrease in spatial resolution (less than 10%) and image texture properties similar to the reference FBP case. Analogous indications were obtained from the analysis on the dedicated test object, revealing a CNR gain from 45% to 100% across different plastic inserts at a comparable or slightly worse spatial resolution and similar NPS peak frequency (difference less than 15%) when compared to FBP. On the other hand, the use of the standard SART algorithm did not provide any advantage over FBP, generally resulting in noisier images and a coarser noise structure. A threshold for NPS frequency peak was used as a first-line discrimination criterion to

Figure 9. F1-score as a function of the CNR for, respectively, (a) gray-level threshold optimization and (b) supervised machine-learning segmentation. Orange and blue open circles indicate cSART reconstructions within and out from the NPS peak threshold condition, black diamond is FBP, and green circle is SART. The magenta squares indicate cSART yielding the highest F1 score for each segmentation method, namely $\sigma_{xy,z} = 2$, $\sigma_v = 0.020$, $w = 0.14$ for the gray-level threshold optimization and $\sigma_{xy,z} = 2$, $\sigma_v = 0.022$, $w = 0.16$ for the supervised machine-learning approach. The dashed vertical line represents the CNR value of the FBP reconstructed reference image at 50 mGy.

identify those cSART parameters that preserve the image texture when compared to FBP. In this study the threshold was arbitrarily set to 15% but, in the future, its definition will be subject to a dedicated reader study. It is worth noting that the triplets of parameters satisfying the threshold condition for the test object overlap with those for the breast specimen.

Moreover, the presence of sharp plastic inserts in the phantom allowed for a TTF analysis, resulting in different trends in the spatial resolution for different materials. This finding further confirms the need for careful optimization of IR algorithms as their performance is dependent on the imaged object, plus it suggests the usefulness of test objects closely reproducing the contrast characteristics of the investigated organ. When the latter condition is satisfied, the similarity among the trends observed in terms of CNR and spatial resolution for breast tissue and the test object, suggests that the optimization of the cSART algorithm can be carried out based on test object images, therefore being feasible virtually in any clinical system. This indication would need to be confirmed by scanning a larger number of samples with a focus on features of clinical interest, such as microcalcifications or margins sharpness. The clinical significance of the improvements brought by the cSART algorithm will be evaluated in a future visual evaluation study performed by qualified readers. Additionally, with the aim of reducing the scan time and (optionally) the radiation dose, the possibility of further exploiting the advantages of cSART will be investigated in scans with a coarser angular sampling.

The study also demonstrated that the proposed algorithm offers great flexibility, allowing for the optimization of image reconstruction either for diagnostic evaluation images (limited CNR gain and textural properties similar to FBP) or for image segmentation (major CNR gain and increased patchiness). The latter feature is of great importance as it would enable, starting from low dose clinical images, accurate glandular fraction estimation and straightforward realization of 3D breast models.

Acknowledgments

Ethical statement

The handling of the specimen followed the Directive 2004/23/EC of the European Parliament and of the Council of 31 March 2004 on setting standards of quality and safety for the donation, procurement, testing, processing, preservation, storage, and distribution of human tissues. The images were acquired in the framework of the operative protocol of the Breast Unit of the Trieste University Hospital ('PDTA Neoplasia mammaria', approved on 11 December 2019 by ASUGIAzienda Sanitaria Universitaria Giuliano Isontina, Italy). Written informed consent was obtained from the patient prior to her inclusion in the study. The specialized breast center of ASUGI is in compliance with the standard of EUSOMA guidelines (certificate No. 1027/01).

ORCID iDs

S Donato ⬤ https://orcid.org/0000-0003-0696-9077
L Brombal ⬤ https://orcid.org/0000-0002-4009-8191
L M Arana Peña ⬤ https://orcid.org/0000-0001-5998-9499
V Fanti ⬤ https://orcid.org/0000-0002-4879-4183
P Oliva ⬤ https://orcid.org/0000-0002-9446-3967

References

Arganda-Carreras I, Kaynig V, Rueden C, Eliceiri K W, Schindelin J, Cardona A and Sebastian Seung H 2017 Trainable weka segmentation: a machine learning tool for microscopy pixel classification *Bioinformatics* **33** 2424–6

Baran P *et al* 2017 Optimization of propagation-based x-ray phase-contrast tomography for breast cancer imaging *Phys. Med. Biol.* **62** 2315

Bartels M 2013 *Cone-Beam x-ray Phase Contrast Tomography of Biological Samples: Optimization of Contrast, Resolution and Field of View* vol 13 (Göttingen, Germany: Universitätsverlag Göttingen) (https://doi.org/10.17875/gup2013-92)

Bellazzini R, Spandre G, Brez A, Minuti M, Pinchera M and Mozzo P 2013 Chromatic x-ray imaging with a fine pitch CdTe sensor coupled to a large area photon counting pixel ASIC *J. Instrum.* **8** C02028

Beltran M A, Paganin D, Uesugi K and Kitchen M J 2010 2D and 3D x-ray phase retrieval of multi-material objects using a single defocus distance *Opt. Express* **18** 6423–36

Bian J, Yang K, Boone J M, Han X, Sidky E Y and Pan X 2014 Investigation of iterative image reconstruction in low-dose breast ct *Phys. Med. Biol.* **59** 2659

Breiman L 2001 Random forests *Mach. Learn.* **45** 5–32

Brombal L 2020a *X-ray phase-contrast tomography: Underlying Physics and Developments for Breast Imaging* (*Springer Theses*) (Cham, Switzerland: Springer Nature) Springer International Publishing (https://doi.org/10.1007/978-3-030-60433-2)

Brombal L 2020b Effectiveness of x-ray phase-contrast tomography: effects of pixel size and magnification on image noise *J. Instrum.* **15** C01005

Brombal L *et al* 2021 Motion artifacts assessment and correction using optical tracking in synchrotron radiation breast ct *Med. Phys.* **48** 5343–55

Brombal L *et al* 2019 Image quality comparison between a phase-contrast synchrotron radiation breast CT and a clinical breast CT: a phantom based study *Sci. Rep.* **9** 1–12

Brombal L, Donato S, Brun F, Delogu P, Fanti V, Oliva P, Rigon L, Di Trapani V, Longo R and Golosio B 2018c Large-area single-photon-counting CdTe detector for synchrotron radiation computed tomography: a dedicated pre-processing procedure *J. Synchrotron Radiat.* **25**

Brombal L *et al* 2018a Phase-contrast breast ct: the effect of propagation distance *Phys. Med. Biol.* **63** 24NT03

Brombal L *et al* 2018b Monochromatic breast computed tomography with synchrotron radiation: phase-contrast and phase-retrieved image comparison and full-volume reconstruction *J. Med. Imaging* **6** 031402

Caballo M, Fedon C, Brombal L, Mann R, Longo R and Sechopoulos I 2018 Development of 3D patient-based super-resolution digital breast phantoms using machine learning *Phys. Med. Biol.* **63** 225017

Chen B, Christianson O, Wilson J M and Samei E 2014b Assessment of volumetric noise and resolution performance for linear and nonlinear CT reconstruction methods *Med. Phys.* **41** 071909

Chen B and Ning R 2002 Cone-beam volume CT breast imaging: feasibility study *Med. Phys.* **29** 755–70

Chen B, Ramirez Giraldo J C, Solomon J and Samei E 2014a Evaluating iterative reconstruction performance in computed tomography *Med. Phys.* **41** 121913

Contillo A, Veronese A, Brombal L, Donato S, Rigon L, Taibi A, Tromba G, Longo R and Arfelli F 2018 A proposal for a quality control protocol in breast CT with synchrotron radiation *Radiol. Oncol.* **52** 329–36

Delogu P, Brombal L, Di Trapani V, Donato S, Bottigli U, Dreossi D, Golosio B, Oliva P, Rigon L and Longo R 2017b Optimization of the equalization procedure for a single-photon counting CdTe detector used for CT *J. Instrum.* **12** C11014

Delogu P, Di Trapani V, Brombal L, Mettivier G, Taibi A and Oliva P 2019 Optimization of the energy for breast monochromatic absorption x-ray Computed Tomography *Sci. Rep.* **9** 1–10

Delogu P *et al* 2017a Imaging study of a phase-sensitive breast-ct system in continuous acquisition mode *J. Instrum.* **12** C01016

Donato S, Brombal L, Arfelli F, Fanti V, Longo R, Oliva P, Rigon L and Golosio B 2019a Optimization of a customized simultaneous algebraic reconstruction technique algorithm for breast ct *2019 IEEE Nuclear Science Symp. and Medical Imaging Conference (NSS/MIC), IEEE* pp 1–2

Donato S, Pacilè S, Brombal L, Tromba G and Longo R 2019b Phase-contrast breast-CT: optimization of experimental parameters and reconstruction algorithms *World Congress on Medical Physics and Biomedical Engineering 2018* (Berlin: Springer) pp 109–15

Euler A, Solomon J, Marin D, Nelson R C and Samei E 2018 A third-generation adaptive statistical iterative reconstruction technique: phantom study of image noise, spatial resolution, lesion detectability, and dose reduction potential *Am. J. Roentgenol.* **210** 1301–8

Fedon C, Longo F, Mettivier G and Longo R 2015 GEANT4 for breast dosimetry: parameters optimization study *Phys. Med. Biol.* **60** N311

Germann M, Shim S, Angst F, Saltybaeva N and Boss A 2020 Spiral breast computed tomography (CT): signal-to-noise and dose optimization using 3D-printed phantoms *Eur. Radiol.* **31** 3693–702

Gervaise A, Osemont B, Lecocq S, Noel A, Micard E, Felblinger J and Blum A 2012 CT image quality improvement using adaptive iterative dose reduction with wide-volume acquisition on 320-detector CT *Eur. Radiol.* **22** 295–301

Ghetti C, Palleri F, Serreli G, Ortenzia O and Ruffini L 2013 Physical characterization of a new CT iterative reconstruction method operating in sinogram space *J. Appl. Clin. Med. Phys.* **14** 263–71

Golosio B, Brunetti A and Cesareo R 2004 Algorithmic techniques for quantitative compton tomography *Nucl. Instrum. Methods Phys. Res. B* **213** 108–11

Gordon R, Bender R and Herman G T 1970 Algebraic reconstruction techniques (art) for three-dimensional electron microscopy and x-ray photography *J. Theor. Biol.* **29** 471–81

Greffier J, Macri F, Larbi A, Fernandez A, Khasanova E, Pereira F, Mekkaoui C and Beregi J 2015 Dose reduction with iterative reconstruction: optimization of CT protocols in clinical practice *Diagn. Interventional Imaging* **96** 477–86

Gureyev T E, Nesterets Y I, Kozlov A, Paganin D M and Quiney H M 2017 On the 'unreasonable' effectiveness of transport of intensity imaging and optical deconvolution *J. Opt. Soc. Am.* A **34** 2251–60

Gureyev T *et al* 2019 Propagation-based x-ray phase-contrast tomography of mastectomy samples using synchrotron radiation *Med. Phys.* **46** 5478–87

Kak A C, Slaney M and Wang G 2002 *Principles of Computerized Tomographic Imaging* (Philadelphia, PA: SIAM) (https://doi.org/10.1137/1.9780898719277)

Kalender W A, Kolditz D, Steiding C, Ruth V, Lück F, Rößler A-C and Wenkel E 2017 Technical feasibility proof for high-resolution low-dose photon-counting CT of the breast *Eur. Radiol.* **27** 1081–6

Li K, Garrett J, Ge Y and Chen G-H 2014 Statistical model based iterative reconstruction (mbir) in clinical CT systems. part ii. experimental assessment of spatial resolution performance *Med. Phys.* **41** 071911

Lindfors K K, Boone J M, Nelson T R, Yang K, Kwan A L and Miller D F 2008 Dedicated breast ct: initial clinical experience *Radiology* **246** 725–33

Lindfors K K, Boone J M, Newell M S and D'Orsi C J 2010 Dedicated breast computed tomography: the optimal cross-sectional imaging solution? *Radiol. Clin.* **48** 1043–54

Lipton Z C, Elkan C and Naryanaswamy B 2014 Optimal thresholding of classifiers to maximize $F1$ measure *Joint European Conf. on Machine Learning and Knowledge Discovery in Databases* (Berlin: Springer) pp 225–39

Longo R *et al* 2019 Advancements towards the implementation of clinical phase-contrast breast computed tomography at Elettra *J. Synchrotron Radiat.* **26** 1343–53

Löve A, Olsson M, Siemund R, StÅlhammar F, Björkman-Burtscher I and Söderberg M 2013 Six iterative reconstruction algorithms in brain CT: a phantom study on image quality at different radiation dose levels *Br. J. Radiol.* **86** 20130388

Makeev A and Glick S J 2013 Investigation of statistical iterative reconstruction for dedicated breast CT *Med. Phys.* **40** 081904

Mettivier G, Fedon C, Di Lillo F, Longo R, Sarno A, Tromba G and Russo P 2015 Glandular dose in breast computed tomography with synchrotron radiation *Phys. Med. Biol.* **61** 569

Miéville F A, Gudinchet F, Brunelle F, Bochud F O and Verdun F R 2013 Iterative reconstruction methods in two different MDCT scanners: physical metrics and 4-alternative forced-choice detectability experiments-a phantom approach *Phys. Med.* **29** 99–110

Mirone A, Brun E and Coan P 2014 A dictionary learning approach with overlap for the low dose computed tomography reconstruction and its vectorial application to differential phase tomography *PLoS One* **9** e114325

Mittone A, Bravin A and Coan P 2018 Low-dose quantitative phase contrast medical CT *Meas. Sci. Technol.* **29** 024006

Mizutani R *et al* 2016 A method for estimating spatial resolution of real image in the Fourier domain *J. Microsc.* **261** 57–66

Nishiyama Y, Tada K, Nishiyama Y, Mori H, Maruyama M, Katsube T, Yamamoto N, Kanayama H, Yamamoto Y and Kitagaki H 2016 Effect of the forward-projected model-based iterative reconstruction solution algorithm on image quality and radiation dose in pediatric cardiac computed tomography *Pediatric Radiol.* **46** 1663–70

O'Connell A, Conover D L, Zhang Y, Seifert P, Logan-Young W, Lin C-F L, Sahler L and Ning R 2010 Cone-beam CT for breast imaging: radiation dose, breast coverage, and image quality *Am. J. Roentgenol.* **195** 496–509

O'Connell A M, Karellas A, Vedantham S and Kawakyu-O'Connor D T 2018 Newer technologies in breast cancer imaging: dedicated cone-beam breast computed tomography *Seminars in Ultrasound, CT and MRI* vol 39 (Amsterdam: Elsevier) pp 106–13

Oliva P *et al* 2020 Experimental optimization of the energy for breast-CT with synchrotron radiation *Sci. Rep.* **10** 1–13

Oliva P *et al* 2017 Quantitative evaluation of breast CT reconstruction by means of figures of merit based on similarity metrics *2017 IEEE Nuclear Science Symp. and Medical Imaging Conference (NSS/MIC), IEEE* pp 1–5

Opitz J and Burst S 2019 Macro $F1$ and macro $F1$ arXiv:1911.03347v2

Pacilè S *et al* 2015 Clinical application of low-dose phase contrast breast CT: methods for the optimization of the reconstruction workflow *Biomed. Opt. Express* **6** 3099–112

Pacilè S *et al* 2019 Free propagation phase-contrast breast ct provides higher image quality than cone-beam breast-ct at low radiation doses: a feasibility study on human mastectomies *Sci. Rep.* **9** 13762

Paganin D, Mayo S C, Gureyev T E, Miller P R and Wilkins S W 2002 Simultaneous phase and amplitude extraction from a single defocused image of a homogeneous object *J. Microsc.* **206** 33–40

Piai A *et al* 2019 Quantitative characterization of breast tissues with dedicated CT imaging *Phys. Med. Biol.* **64** 155011

Polan D F, Brady S L and Kaufman R A 2016 Tissue segmentation of computed tomography images using a random forest algorithm: a feasibility study *Phys. Med. Biol.* **61** 6553

Richard S, Husarik D B, Yadava G, Murphy S N and Samei E 2012 Towards task-based assessment of CT performance: system and object MTF across different reconstruction algorithms *Med. Phys.* **39** 4115–22

Rodrigues É O, Morais F, Morais N, Conci L, Neto L and Conci A 2016 A novel approach for the automated segmentation and volume quantification of cardiac fats on computed tomography *Comput. Methods Programs Biomed.* **123** 109–28

Saiga R, Takeuchi A, Uesugi K, Terada Y, Suzuki Y and Mizutani R 2018 Method for estimating modulation transfer function from sample images *Micron* **105** 64–9

Sarno A, Mettivier G and Russo P 2015 Dedicated breast computed tomography: basic aspects *Med. Phys.* **42** 2786–804

Schindelin J *et al* 2012 Fiji: an open-source platform for biological-image analysis *Nat. Methods* **9** 676–82

Schulz B, Beeres M, Bodelle B, Bauer R, Al-Butmeh F, Thalhammer A, Vogl T and Kerl J 2013 Performance of iterative image reconstruction in CT of the paranasal sinuses: a phantom study *Am. J. Neuroradiol.* **34** 1072–6

Shim S, Saltybaeva N, Berger N, Marcon M, Alkadhi H and Boss A 2020 Lesion detectability and radiation dose in spiral breast CT with photon-counting detector technology: A phantom study *Investigative Radiol.* **55** 515–23

Sidky E Y, Chartrand R, Boone J M and Pan X 2014 Constrained TpV minimization for enhanced exploitation of gradient sparsity: Application to CT image reconstruction *IEEE J. Translational Eng. Health and Med.* **2** 1–18

Sidky E Y and Pan X 2008 Image reconstruction in circular cone-beam computed tomography by constrained, total-variation minimization *Phys. Med. Biol.* **53** 4777

Solomon J, Marin D, Roy Choudhury K, Patel B and Samei E 2017 Effect of radiation dose reduction and reconstruction algorithm on image noise, contrast, resolution, and detectability of subtle hypoattenuating liver lesions at multidetector CT: filtered back projection versus a commercial model-based iterative reconstruction algorithm *Radiology* **284** 777–87

Solomon J, Wilson J and Samei E 2015 Characteristic image quality of a third generation dual-source MDCT scanner: noise, resolution, and detectability *Med. Phys.* **42** 4941–53

Taylor J A 2018 TS imaging (http://ts-imaging.science.unimelb.edu.au/Services/Simple/)

Thompson D A, Nesterets Y I, Pavlov K M and Gureyev T E 2019 Fast three-dimensional phase retrieval in propagation-based x-ray tomography *J. Synchrotron Radiat.* **26** 825–38

Tromba G *et al* 2010 The syrmep beamline of elettra: clinical mammography and bio-medical applications *AIP Conf. Proc.* **1266** 18–23

Tseng H W, Vedantham S and Karellas A 2020 Cone-beam breast computed tomography using ultra-fast image reconstruction with constrained, total-variation minimization for suppression of artifacts *Phys. Med.* **73** 117–24

Van Aarle W, Palenstijn W J, Cant J, Janssens E, Bleichrodt F, Dabravolski A, De Beenhouwer J, Batenburg K J and Sijbers J 2016 Fast and flexible x-ray tomography using the Astra toolbox *Opt. Express* **24** 25129–47

Verdun F *et al* 2015 Image quality in CT : From physical measurements to model observers *Phys. Med.* **31** 823–43

White D, Booz J, Griffith R, Spokas J and Wilson I 1989 *Tissue Substitutes in Radiation Dosimetry and Measurement, Report* 44 Commission on Radiation Units &Measurements, Bethesda, MD, USA (https://doi.org/10.1093/jicru/os231.)

Wienbeck S, Lotz J and Fischer U 2017 Review of clinical studies and first clinical experiences with a commercially available cone-beam breast CT in europe *Clin. Imaging* **42** 50–9

Wilkins S, Gureyev T E, Gao D, Pogany A and Stevenson A 1996 Phase-contrast imaging using polychromatic hard x-rays *Nature* **384** 335–8

Willemink M J, Leiner T, de Jong P A, de Heer L M, Nievelstein R A, Schilham A M and Budde R P 2013 Iterative reconstruction techniques for computed tomography part 2: initial results in dose reduction and image quality *Eur. Radiol.* **23** 1632–42

Wollatz L, Johnston S J, Lackie P M and Cox S J 2017 3d histopathologya lung tissue segmentation workflow for microfocus x-ray-computed tomography scans *J. Digital Imaging* **30** 772–81

Wu X-Z and Zhou Z-H 2017 A unified view of multi-label performance measures *Int. Conf. on Machine Learning* (PMLR) pp 3780–8

Zhao Y *et al* 2012 High-resolution, low-dose phase contrast x-ray tomography for 3D diagnosis of human breast cancers *Proc. Natl Acad. Sci.* **109** 18290–4